Effect of an electric field on ferroelectric and piezoelectric properties of brownmillerite $Ca_2Al_2O_5$

R. Arras [1,*] C. Paillard [2] and L. Bellaiche [3]

[1] *CEMES, Université de Toulouse, CNRS, 29 rue Jeanne Marvig, F-31055 Toulouse, France*

[2] *Université Paris-Saclay, CentraleSupélec, CNRS, Laboratoire SPMS, 91190 Gif-sur-Yvette, France*

[3] *Physics Department and Institute for Nanoscience and Engineering, University of Arkansas, Fayetteville, Arkansas 72701, USA*

(Received 18 February 2023; revised 5 April 2023; accepted 6 April 2023; published 20 April 2023)

Brownmillerites $A_2B_2O_5$ are oxides possessing a crystallographic structure that is parent from the perovskite structure ABO_3 with an ordered sublattice of oxygen vacancies, forming a network of one-dimensional chiral chains of oxygen tetrahedra carrying electric dipoles. The distribution of left-and right-handed chains enables the formation of different, polar or nonpolar, crystallographic phases with close internal energies. We have performed first-principles calculations on the nonmagnetic $Ca_2Al_2O_5$ oxide, chosen as a case study, in order to investigate the effect of an external electric field, applied in the direction parallel to the chains, on the stability of four different crystallographic phases. We found that reversing the direction of the electric polarization in the *Ima*2 phase necessitates going through different intermediate phases. However, we also showed that, even if the application of the electric field allows to change the relative stability of each phase, it cannot be sufficient to change one-chain handedness at low temperature, owing to the high barrier energies, of the order of ∼1 eV per chain of two tetrahedra, which has to be overpassed. Switching between different phases would thus require applying an electric field at high temperature or with the application of additional stress. Finally, we demonstrated that polar phases, such as *Ima*2 or $Pmc2_1$, display negative longitudinal piezoelectric coefficients due to the lattice response to the applied electric field.

DOI: 10.1103/PhysRevB.107.144107

I. INTRODUCTION

Brownmillerite oxides of chemical formula $A_2B_2O_5$ (or, equivalently, $ABO_{2.5}$) possess a structure similar to the structure of perovskite oxides (of chemical formula ABO_3) in which oxygen vacancies are ordered and form one-dimensional (1D) channels, all aligned along a specific crystallographic direction. These oxides have already shown a wide range of properties because of the numerous combinations of *A* and *B* cations which can be used to new compounds [1,2] with different lattice distortions, oxidation states, and magnetic ordering, providing a large range of functional properties. Hence, this family of oxides could help to enrich the list of multifunctional materials. Multiferroicity has, for example, been evidenced in materials such as $SrFeO_{2.5}$ [3] and studied theoretically in $Ca_2(Fe,Al)O_5$ [4]. Brownmillerites are nowadays increasingly studied and could be as promising as their perovskite parents for future applications.

The particular tunabilities of brownmillerite properties are generally explained by the configurations of the chains of oxygen tetrahedra (*T* chains) formed because of the oxygen-vacancy channels. Similarly to the octahedra tilts observed in perovskite oxides, the oxygen tetrahedra can display tilts which make the associated chains to be chiral. Different control parameters and stimuli (chemical composition, temperature, strain, applied electric field) can be used to tune the atomic structure by changing the tetrahedra-tilts pattern [4,5], the *T*-chain crystallographic orientations [6–8], or the oxygen content through topotactic phase transitions ($ABO_{2.5}$ brownmillerites being an intermediate structure between ABO_3 perovskites and ABO_2 structures with infinite square lattices) [7,9–13], all of this resulting in modifications of electronic, optical, and magnetic properties. Topotactic transitions through brownmillerite structures are in particular promising for memristive devices and neuromorphism computing [7,8,13–15], as the anisotropic mobility of oxygen atoms is facilitated along the oxygen-vacancy channel, which moreover reduces the variability of the switching mechanisms [15].

If several research efforts have been dedicated to the study of topotactic transitions, the ordering of oxygen-tetrahedra tilts between different *T* chains remains an important characteristic of brownmillerites, as it is intimately linked to the possible emergence of a ferroelectric polarization in these oxides [3–5,16]. Brownmillerites indeed display a nonconventional ferroelectricity, which comes from cation-oxygen displacements resulting from these oxygen-tetrahedra tilts. The collective tilts in each *T* chain result in left- or right-handed chiralities (noted "−" and "+" in the following) and are responsible of the emergence of electric dipoles along the [010] direction, the signs of which are defined by the chiral orientation of the *T* chains. The distribution of the orientations of the different chains will determine the value of the macroscopic electric polarization [16]. Finally, confirming the complexity of this system, Tian *et al.* [17] demonstrated that the ferroelectric state in the $Pmc2_1$ ground state of $Sr_2Co_2O_5$ originates from a novel coupling between different phonon

*remi.arras@cemes.fr

modes, which differ from those characteristic of the proper, improper [18], hybrid improper [19–22], or triggered [23,24] type of ferroelectricity.

The chemical composition is the first important criterion to explain the stabilization of a particular (polar or nonpolar) crystallographic phase. From a series of measurements on $La_{1-x}A_xMnO_{2.5}$ (with A = Ba, Sr, Ca), Parsons *et al.* [16] showed that the chain handedness ordering can be tuned by changing the chemical composition of A cation *via* two effects. First, by changing the interlayer distances between two (001) T atomic layers. Second, by modifying the distortions on the T chains, which is a result of the change of Mn oxidation degrees in octahedral sites. Different structures can thus be generated as a function of the tilts patterns. The *Ima*2 structure, which corresponds to the case with all T chains having the same handedness, can be stable when the net electric dipole is small. When electric dipole is too large, a centrosymmetric structure will form to compensate it: the structure will then possess an intralayer antiferroelectric ordering (*Pbcm*) if the separation distance between two adjacent T layers is large, while it will favor an interlayer antiferroelectric ordering otherwise, as such ordering does not involve a strong distortion of the oxygen octahedra [16,25,26]. In this latter case a *Pnma* structure will form, with all tetrahedra T chains in T and T' layers having chains with opposite chiralities. More generally, explanations of the structural ground states have been given through the use of several structural descriptors characterizing the distortions in terms of chemical bond angles and length changes [5,16]. For certain brownmillerites, or when the temperature is increased, the chain orientations can be disordered, leading to an *Imma* structure and (3+1)-dimensional [(3+1)D] $Imma(00\gamma)s00$ superspace groups have even been often characterized to describe the formation of incommensurate orderings [27–29]. In addition to the choice of chemical composition, it has been found that the physical control of phases in brownmillerites is strongly dependent on the strain [5].

Applying an external electric field would be another way to modify the brownmillerite structure and properties. Experimentally, it has been shown that it could help to modify the T-chain crystallographic orientation [7] or to activate the oxygen conduction [7,8,15]. To our knowledge, no study has been reported on the effect of an electric field on the oxygen-tetrahedra tilts and of the T-chain handedness pattern, despite the fact that, as demonstrated in the case of perovskites [30], this would be important to understand the modification of ferroelectric properties, in view of integrating such materials in electronic devices.

In this paper, we show how the electric polarization can be reversed or tuned by an applied electric field in $Ca_2Al_2O_5$. We demonstrate that the electric field mostly induces an additional contribution to the polarization by displacing cations and anions in directions parallel or antiparallel to the electric field, while the tetrahedra-tilt patterns remain robust. We also show that the reversal of the spontaneous electric polarization is not homogeneous and requires to overcome high-energy barriers. Finally, we discuss the lattice-strain response to the electric field which is linked to a longitudinal negative piezoelectric coefficient.

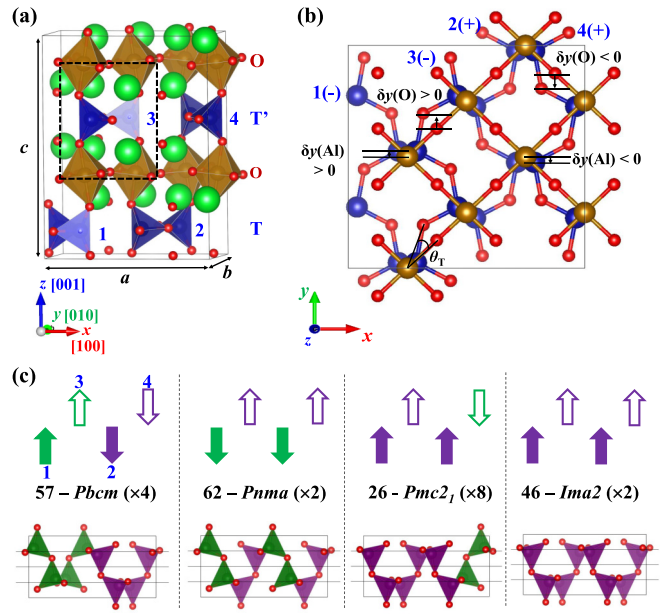

FIG. 1. (a) Side and (b) bottom views of the brownmillerite structure with a $2\sqrt{2} \times \sqrt{2} \times 4$ supercell. The displayed structure corresponds to the most stable *Pbcm* space group, with two tetrahedra chains (in blue) having opposite chiralities in each (001) T atomic layers along the c axis. For the sake of clarity, we represented two cell periods along the y direction in (b). (c) Atomic structures of the four more stable crystallographic structures generated from the different chiral-state patterns (12|34). The structures correspond to a projection onto the (001) plane and only the chains of tetrahedra are shown. The green and purple arrows give the orientation of the electric dipoles along the [010] direction; plain and empty arrows correspond to dipoles located in different (001) atomic layers. The black lines help to visualize the atomic displacements δy(Al) and δy(O) according to the centrosymmetric positions. The multiplicity of each structure is given between parentheses.

II. DETAILS ON THE CALCULATION METHODS AND ON THE BROWNMILLERITE STRUCTURE

We performed first-principles calculations based on the density functional theory (DFT) [31,32], using the VASP software [33,34]. We employed the projector augmented wave method (PAW) [35] with a cutoff energy of 550 eV. The exchange-correlation functional was expressed within the generalized-gradient approximation parametrized by Perdew, Burke, and Ernzerhof and revised for solids (GGA-PBESol) [36]. The first Brillouin zone was sampled using a Monkhorst-Pack grid [37] with dimensions $4 \times 6 \times 2$.

The external electric field is applied using the method proposed in Ref. [30]. The stability of the atomic structure is then governed by the energy F, which is, at a temperature of 0 K, equal to the Kohn-Sham internal energy U plus an additional electric-field- ($\mathcal{E}$-) dependent contribution, such that $F = U - \boldsymbol{P} \cdot \boldsymbol{\mathcal{E}}$. The electric polarization P has been calculated using the Born effective charges Z^* (calculated for the centrosymmetric *Imma* phase and given in Appendix A); this method is also convenient as it allows to perform a projection in a given volume [illustrated by the black dotted lines in Fig. 1(a)] to separate each T-chain contribution. For some

polar bulk structures, we also calculated the total electric polarization using the Berry-phase method and found a fairly good agreement between the results obtained with both methods. To optimize the atomic structures, we calculated the total forces applied on each atom, which are now the sum of the standard Hellmann-Feynman forces plus a product between its Born effective charge Z^* and the electric field $\mathcal{E}$. To calculate the barrier energy to switch between two structural states, we used the climbing-image nudged elastic band method (CI-NEB) implemented within the VTST package [38].

The brownmillerite structure corresponds to a perovskite structure with oxygen vacancies aligned along the $[110]_p$ direction (we denote by "p" the directions and lattice parameters of a perovskite cell, while, when no precisions are given, the lattice parameters are those of the brownmillerite structure), which corresponds to the [010] direction (denoted as the y axis in Fig. 1) in the brownmillerite structure [1,16]. Along the [001] (or equivalently $[001]_p$) direction, the structure is composed by an alternation of layers with B cations located either in octahedra (O) or in tetrahedra (T) atomic sites formed by the sublattice of oxygen atoms and separated by atomic planes with A cations. The successive (001) atomic layers thus have the chemical composition AO-BO_2-AO-BO; if we only consider the layers containing B cations, the structure corresponds to the sequence $OTOT'$, with T and T' being two atomic layers with oxygen tetrahedra shifted one to each other along the $[1\bar{1}0]_p$ (or [100]) direction [see Fig. 1(a)]. Because of the oxygen-vacancies ordering, the oxygen tetrahedra in the T and T' layers form so-called *zweier* single chains [28] oriented along a $\langle 110\rangle_p$ direction and associated with oxygen-vacancy channels. The studied structures are orthorhombic with lattice parameters $a \simeq 2\sqrt{2}a_p$, $b \simeq \sqrt{2}b_p$, and $c = 4c_p$, with a, b, and c being, respectively, along the $[1\bar{1}0]_p$, $[110]_p$, and $[001]_p$ directions. With these new basis vectors, the tetrahedra chains are oriented along the [010] direction, i.e., the y axis. The given supercell contains eight formula units (f.u.) of $Ca_2Al_2O_5$ and four T chains of two tetrahedra.

III. RESULTS

A. Properties of bulk $Ca_2Al_2O_5$ brownmillerite

We chose to focus our study on the $Ca_2Al_2O_5$ brownmillerite [29,39,40]. This oxide has not been extensively studied but it possesses the advantages to contain only one type of cation A and one type of cation B with both being nonmagnetic. It is derived from the native $Ca_2(Fe_{1-x}Al_x)_2O_5$ brownmillerite, which has been found to naturally exist and which can be grown at ambient pressures for compositions x ranging from $x = 0$ to 0.7 [41,42]. Al-rich phases of $Ca_2(Fe_{1-x}Al_x)_2O_5$ generally adopt a *Ima*2 (or *I*2*mb*) space group [29,40], while iron-rich phases (below $x = 0.235$) have been reported with a *Pnma* structure [28,43]. Both for Al-rich or Fe-rich phases, a transition to an incommensurate structure, with a superspace group (3+1)D $Imma(00\gamma)s00$, has been evidenced at high temperature [28,29]. The experimental synthesis of $Ca_2Al_2O_5$ (that is for $x = 1$) requires high pressure and high temperature, and it is then possible to quench the material at room temperature (see Ref. [29] and references therein) in order that the system stays in the brownmillerite structure.

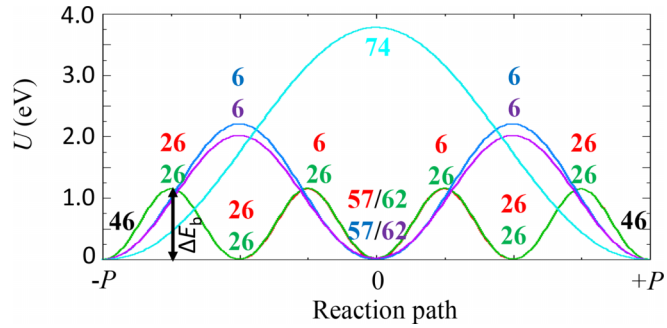

FIG. 2. Barrier energies calculated to switch between two *Ima*2 phases with electric polarization equal to $-P$ and to $+P$. Several reaction paths, involving different intermediate crystallographic phases, are shown: by switching the chains one by one [46 → 26 → 57 → 26 → 46 (red) and 46 → 26 → 62 → 26 → 46 (green)], two by two [46 → 57 → 46 (dark blue) and 46 → 62 → 46 (purple)], and all at the same time [46 → 46 (cyan)]. The numbers given above the curves correspond to the space groups adopted during the reaction path at each maximum and minimum. Because of their relatively close energies, the red and green curves are almost superimposed. The barrier energies are calculated using the supercell presented in Fig. 1(a), in which a T chain period is formed by two AlO_4 tetrahedra. The atomic structures associated to the red curve can be seen in Fig. 8.

1. *Stability of the different crystallographic phases*

$Ca_2Al_2O_5$ can exist under different crystallographic phases, which differ one from another by their pattern of chain handedness. With our considered supercells, these patterns of chain handedness will be noted (12|34), where 1–4 are the chain numbers given in Fig. 1. The right- or left-handed enantiomorphic chains will be noted + and −, respectively, and 0 will correspond to an average state, when the tetrahedra display no rotation.

The aristotype *Imma* space group (No. 74) corresponds to the brownmillerite structure (12|34) = (00|00) with no tetrahedra tilts. Using the supercell described in the previous section, it is then possible to generate four hettotype structures, as shown in Fig. 1(c). Table I summarizes the main properties of each of these structures.

The *Ima*2 structure (No. 46) is noncentrosymmetric and possesses only T chains with one specific handedness ("−" or "+") defined from the tetrahedra-tilts direction. This structure thus displays a spontaneous electric polarization that we calculated to be $P^0_{tot} = 3.8$ μC cm^{-2} by using Born effective charges; a slightly lower value of 3.6 μC cm^{-2} was obtained using the Berry-phase method. By changing the intralayer relative chain direction, it is possible to switch from this *Ima*2 structure (++|++) to the *Pbcm* nonpolar structure (+−|+−) (No. 57), which corresponds to our calculated ground-state structure and which is more stable than the *Ima*2 structure by 0.08 meV/f.u. according to our simulations. Still from the *Ima*2 polar structure, it is also possible to generate the less stable centrosymmetric *Pnma* structure (−−|++) (No. 62), by modifying the interlayer ordering. Finally, the

TABLE I. Lattice parameters (a, b, c), averaged tetrahedra tilts $\langle|\theta_T|\rangle$, local and total electric polarizations P_α and P^0_{tot}, and internal energy U per formula unit of $Ca_2Al_2O_5$. The zero of energy is chosen for the ground state, *Pbcm*.

Space group		Chiral states	a	b	c	$\langle\|\theta_T\|\rangle$	$\langle\Delta y_T\rangle$	P_α				P^0_{tot}	U
			(Å)	(Å)	(Å)	(°)	Å	μC cm^{-2}				μC cm^{-2}	meV/f.u.
Number	Name							1	2	3	4		
74	*Imma*	(00|00)	10.8223	5.3603	14.0670	0.00	0.00	0.00	0.00	0.00	0.00	0.00	468.55
57	*Pbcm*	(+ − | + −)	10.8093	5.2306	14.3532	25.73	0.00	0.86	−0.86	0.86	−0.86	0.00	0.00
62	*Pnma*	(− − | + +)	10.8123	5.2274	14.3593	25.63	0.00	1.02	1.02	−1.02	−1.02	0.00	2.92
26	$Pmc2_1$	(+ − | + +)	10.8115	5.2288	14.3539	25.67	0.23	0.99	0.99	0.82	−0.90	1.90	0.89
46	*Ima*2	(+ + | + +)	10.8144	5.2280	14.3489	25.61	0.46	0.96	0.96	0.96	0.96	3.85	0.08
46	*Ima*2[a]	(+ + | + +)	10.8008	5.2281	14.4686								
74.2	$Imma(00\gamma)s00$[b]		10.8392	5.2699	14.6984								

[a]Experimental, measured at room temperature [40].
[b]Experimental, measured at $T = 1090$ K [29].

intermediate $Pmc2_1$ structure (+ − | + +) (No. 26), associated with an electric polarization of 1.9 μC cm^{-2} (1.2 μC cm^{-2} with the Berry-phase method), is obtained by changing the tilts direction in only one chain from the three previous structures (*Ima*2, *Pnma*, and *Pbcm*). To summarize, with a brownmillerite supercell with four T chains, it is possible to generate four nonequivalent structures. It is important to note that different tilts patterns can correspond to the same structure, the four structures *Ima*2, $Pmc2_1$, *Pbcm*, and *Pnma* hence having a multiplicity of 2, 8, 4, and 2, respectively.

From Table I, we can see that the calculated lattice parameters are in fairly good agreement with reported experimental parameters, with a calculated pseudocubic lattice parameter for the *Ima*2 phase only 0.23% lower than the experimental value [40]. From our calculations, we can also see that the variation of lattice parameters between the different crystallographic phases is quite small for the four more stable phases (−0.01% in average between the *Pbcm* and *Ima*2 phases), while it is more important if we consider the *Imma* phase (−0.19% with the *Pbcm* phase). The larger lattice distortion separating the *Imma* phase from the four other structures is in agreement with the calculated high internal energy. The in-plane distance separating two T chains only decreases by 0.26 pm when changing from the *Ima*2 to the *Pbcm* phase, while the out-of-plane distance increases by 0.52 pm when switching from the *Ima*2 to the *Pnma* phase. For the four structures, *Ima*2, $Pmc2_1$, *Pnma*, and *Pbcm*, the averaged absolute value of the tetrahedra-tilt angles $\langle|\theta_{yT}|\rangle$ does not strongly vary and remains in the range of 25.61°–25.73°. Depending on the handedness of the T chain, the Al cations and anions are all displaced in the same direction along the y axis. For example, in the case of the *Ima*2 structure, we found that the Al atoms are, in average, displaced from their centrosymmetric positions by $\delta y(\mathrm{Al}) = -18.4$ pm, and the oxygen atoms by $\delta y(\mathrm{O}) = -64.5$ pm, so that the cation-oxygen buckling is of $\Delta y_T(Ima2) = \delta y(\mathrm{Al}) - \delta y(\mathrm{O}) = 46.1$ pm. The spontaneous electric polarization is really dependent on the distortions located in the T and T' layers; if we calculate a similar averaged oxygen-cation buckling in the O layer, we indeed find a much lower buckling of $\langle\Delta y_O(Ima2)\rangle \simeq 0.7$ pm. In the case of the *Pbcm* phase, we calculated larger atomic displacements $\delta y(\mathrm{O}) = \pm 72.2$ pm and $\delta y(\mathrm{Al}) = \pm 26.0$ pm (the sign depends on the considered chain and its handedness), which, however, still correspond to a similar cation-oxygen buckling, in a given chain, of $\Delta y_T(Pbcm) = \pm 46.2$ pm. The buckling values $\langle\Delta y_T\rangle$ averaged on the four T chains follow the same trends as the electric polarization, which is proportional to the number of + and − chains.

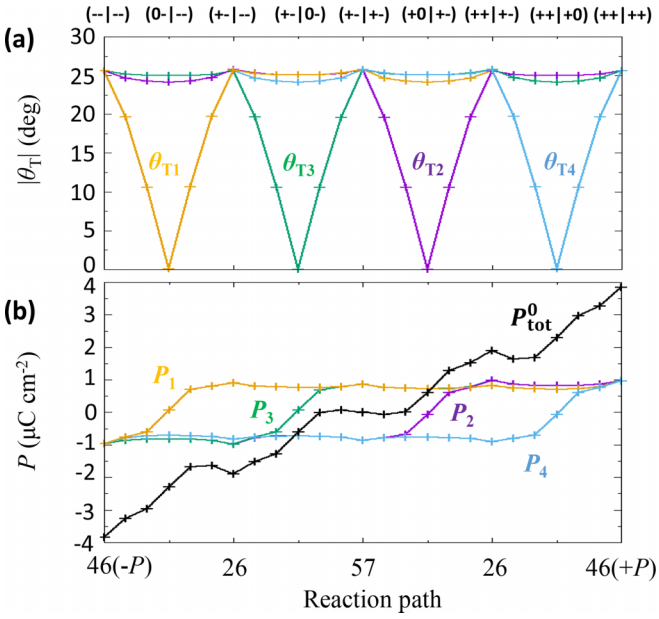

FIG. 3. Variations of (a) tilt angles $|\theta_T|$ and (b) local electric polarization P_α associated to the T chains (12|34) along the reaction path 46 → 26 → 57 → 26 → 46 (red curve in Fig. 2). The local electric polarization P_α are calculated by summing the contributions of atoms located in a volume centered around a given T chain and as defined by the black dotted lines of Fig. 1(a).

2. *Energy barrier to switch between the different phases*

The NEB method was used to calculate the energy barrier ΔE_b which has to be overcome to reverse the electric polarization in the case where the *Ima*2 phase is stabilized. $\Delta E_b(\alpha \to \beta)$ is defined as the energy difference between

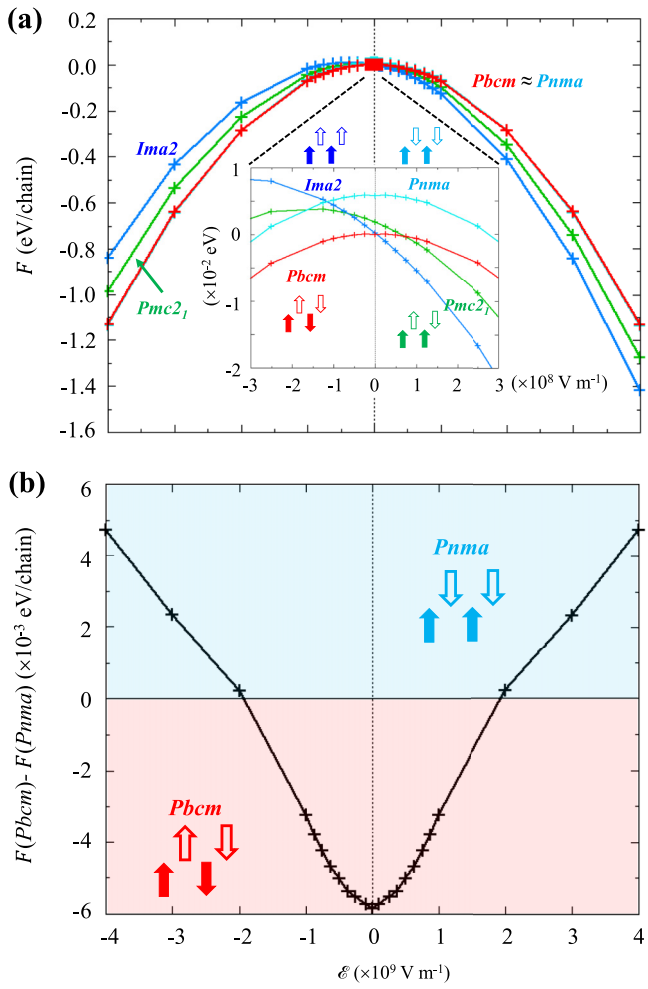

FIG. 4. (a) Free energy F as a function of the electric field $\mathcal{E}$ applied to the four studied crystallographic phases of $Ca_2Al_2O_5$. (b) Difference of free energies calculated between the *Pbcm* and *Pnma* phases. As in Fig. 1(c), the arrows indicate the configuration of electric dipoles in each crystallographic phase.

the maximum of the energy calculated along a reaction path between two states α and β and the energy of the initial state α.

A homogeneous switching, corresponding to a direct $46 \rightarrow 46$ transition, would require to rotate simultaneously all T chains and the maximum of the energy barrier would be reached when all tetrahedra tilts $\theta_T = 0°$, i.e., when the structure takes the *Imma* space group. In that case, as displayed in Fig. 2, the total energy barrier for the whole heterostructure is thus expected to be $\Delta E_b(46 \rightarrow 46) = 3.78$ eV, or 0.95 eV per chain of two tetrahedra. Such energy barrier is high if we compare it to common ferroelectric materials for which the energy required to switch the electric polarization is in the order of tens of meV [44]. On the other hand, our calculated value is closer to the energy barriers reported for geometric ferroelectrics [21], in which the ferroelectricity is driven by rotations and it is approximately three times higher than the value calculated for the Brownmillerite $Sr_2Fe_2O_5$ [3]. The high energy necessary to change the T-chain handedness may be easily understood from geometry considerations, taking into account that a T chain is formed by a succession of oxygen tetrahedra turning alternatively in clockwise and anticlockwise directions and changing the chain handedness would require to reverse simultaneously the angles of all tetrahedra. It is important to note that these calculated energy barriers are of the same order of magnitude than those calculated for the migration of oxygen atoms between different atomic sites [15,45].

Up to now, we considered that the polarization reversal was performed by homogeneously switching all chains at the same time. It is, however, reasonable to assume that the polarization switching would rather occur by changing the handedness of the T chains one after another, eventually through the motions of domain walls [44,46]. Locally, such process could allow to generate different intermediate states corresponding to phases like those discussed before. For this reason, we also calculated the energy barriers to transit between the different phases by switching only one or two chains at the same time. Because of the distortions induced in the structure in the near environment of the chain with rotating tetrahedra and the structural connections with other chains, rotating separately the chains increases slightly the chain barrier energy to 1.10 and 1.15 eV per chain of two tetrahedra, if two or one chains are rotating at the same time, respectively (these energies are always given according to the energy of the *Ima*2 phase). We can indeed see in Fig. 3(a) that rotating oxygen tetrahedra in a specific chain (e.g., chain 1) induces also a very small variation of tilt angles in the chain belonging to the same (001) atomic layer (i.e., chain 2). This may also explain why the energy barrier $\Delta E_b(62 \rightarrow 46)$ is lower by 21 meV than the barrier $\Delta E_b(57 \rightarrow 46)$. The structural coupling between the different T chains and the induced structural distortions are, however, relatively low and, in a first approximation, we can consider that each chain behaves almost independently: as discussed before and displayed in Fig. 3(b), each chain-state reversal increases approximately the total electric polarization by, in average, $P_\alpha \simeq 0.94$ μC cm^{-2}. This result is in agreement with the relation $P^0_{tot}(Ima2) = 2P^0_{tot}(Pmc2_1)$ linking the polarizations calculated for the two polar states and with the individual chain contributions P_α to the total polarization displayed in Table I, which only vary by ±8.5% in magnitude, depending on the states of the surrounding chains.

B. Effect of an electric field parallel to the chains

Since the spontaneous electric polarization in the brownmillerite structure depends on the tilt pattern, we tried to verify if it is possible to change the rotation direction of the T chains, and therefore to switch between different crystallographic phases by applying an electric field. Our calculations were performed by adding the effect of an electric field ranging from -4×10^9 to 4×10^9 V m^{-1} and oriented along the *b*[010] axis, i.e., the direction of the electric dipoles in the four phases *Pbcm*, *Pnma*, *Ima*2, and *Pmc*2_1. Because the electric field is applied in the direction (anti)parallel to the electric polarization of the polar phases, their space group will remain the same; on the contrary, the electric field will break the inversion symmetry of nonpolar phases and the *Pnma* structure will turn in a structure with the *Pmc*2_1 space group, while the *Pbcm* structure will transform into *Pma*2 (No. 28). For the

sake of simplicity, we will continue to call the structure using their space group at zero field.

1. Thermodynamic stability

In Fig. 4(a), we display the evolution of the free energy F calculated for the different crystallographic phases and as a function of the applied electric field $\mathcal{E}$. First of all, we can notice that the variation of F is symmetrical for the nonpolar phases *Pbcm* and *Pnma*, while it is not the case for the polar phases *Ima*2 and $Pmc2_1$, for which the value of the free energy depends on the direction of the electric field, which can be parallel (positive values) or antiparallel (negative) to the spontaneous polarization P^0_{tot} calculated at zero field.

As discussed in the previous section, when no electric field is applied, the nonpolar *Pbcm* phase corresponds to the ground state, but it displays only a rather small energy difference, of 0.08 meV/f.u., with the second most stable phase, which is the polar *Ima*2 structure. In the presence of a parallel external electric field with a magnitude greater than $\mathcal{E} = +4.6 \times 10^6$ V m^{-1}, this polar phase becomes more stable, and the intermediate (and also polar) $Pmc2_1$ phase the second most stable from $\mathcal{E} = +7.2 \times 10^7$ V m^{-1}. On the contrary, it can be seen that, if the electric field is applied antiparallel, the two nonpolar phases not only remain the more stable states, but their energy difference with respect to the energies of the polar phases increases with the magnitude of $\mathcal{E}$.

Comparing the two nonpolar phases, we can see in Fig. 4(a) that the two curves representing the variation of their free energy are almost superimposed, which shows that their energy difference remains low, in comparison with the energy difference with other phases, even at high electric-field values. In Fig. 4(b), we can indeed see that the energy difference between these two nonpolar phases is at most 5.8 meV/chain of two tetrahedra. From this figure, we can also see that the energy difference between these two phases as a function of $\mathcal{E}$ is not really constant and it appears that the *Pnma* structure becomes the most stable structure above $|\mathcal{E}| = 1.9 \times 10^9$ V m^{-1}.

If we come back to the energy path $46(-P) \rightarrow 26 \rightarrow 57 \rightarrow 26 \rightarrow 46(+P)$ calculated in Fig. 2 (red curve), we can wonder how the calculated energy barriers ΔE_b vary when an electric field of $\mathcal{E} = +10^8$ V m^{-1} (antiparallel to the initial polarization $-P$) is applied. As shown in Fig. 5, we found that these barriers will be reduced by at most ∼9 meV when switching between the 46-*Ima*2 and the 26-$Pmc2_1$ phases, and by ∼1 meV between the 26-$Pmc2_1$ and 57-*Pbcm* phases, which corresponds to a maximum reduction of only 0.75% if compared to the energy barrier without any electric field. Because higher electric fields can be experimentally applied in thin films, we calculated the barrier energies for higher magnitudes of $\mathcal{E}$: The energy barriers to switch the electric dipoles on one T chain become more homogeneous as we increase $\mathcal{E}$, but they remain very high, of around 1.092 eV when the electric field is of $+5 \times 10^8$ V m^{-1} and that the global electric polarization is still antiparallel to it, and 1.114 eV, when the electric field and the electric polarization are parallel.

According to our calculations, it appears that, even by applying a large electric field, it should be difficult to switch between different crystallographic phases, at least at a temperature of 0 K. It is nonetheless interesting that Kang *et al.* [3] demonstrated the possibility to reverse the electric polarization at room temperature in a thin film of $Sr_2Fe_2O_5$ in its *Ima*2 ferroelectric phase; they estimated that the electric coercive field was about 1.5×10^8 V m^{-1}. The ability to reverse the electric polarization with such an electric field might highlight the importance of domain-wall motion in the polarization-switching mechanism of brownmillerites.

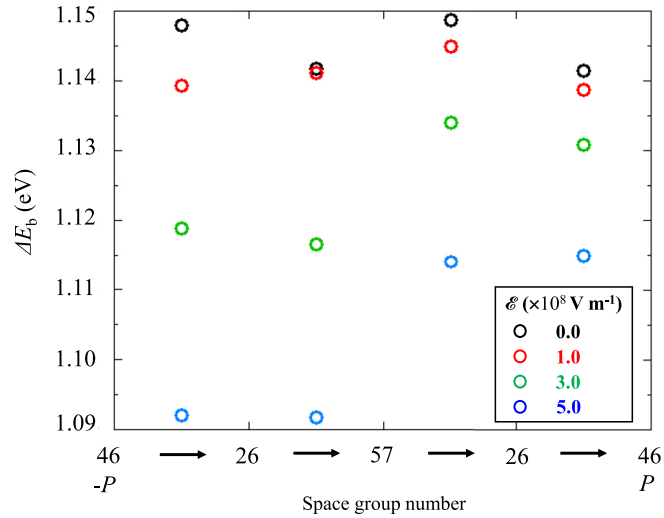

FIG. 5. Energy barriers to switch between the different indicated crystallographic phases and to fully reverse the electric polarization of the *Ima*2 phase, with/without an applied electric field of 10^8 to 5×10^8 V m^{-1}.

Finally, we can also address the idea that, if the system is initially in a nonpolar state, it could be possible to stabilize the polar phase *Ima*2 by heating the sample and by applying the electric field at a sufficiently high temperature; if we then slowly cool down the system in order to keep it in equilibrium in the polar *Ima*2 phase, we can expect to preserve this state down to room temperature. This state should then be locked, even after removing the electric field.

2. Evolution of the electric polarization

From the NEB calculations described previously, we saw that the energy cost to reverse the T-chain handednesses, which are linked to the spontaneous electric polarization P^0_{tot} at zero electric field, is very high. The electric field applied in our calculations will nonetheless modify the atomic structure and induce an additional contribution to the electric polarization. As displayed in Figs. 6(a) and 6(b), the total electric polarization is increasing quasilinearly, as a function of the electric field, between $\mathcal{E} = -10^9$ and $+10^9$ V m^{-1}, with a slope of 11.24×10^{-11} F m^{-1} and 11.04×10^{-11} Fm^{-1}, for the polar *Ima*2 and non-polar *Pbcm* phase, respectively. We calculated similar dielectric response (not shown) for the two other phases, with $\frac{dP_{\text{tot}}}{d\mathcal{E}} = 11.39 \times 10^{-11}$ F m^{-1} for the *Pnma* phase and 11.20×10^{-11} F m^{-1} for the $Pmc2_1$ one. An additional cubic contribution ranging from -0.065×10^{-10} F m V^{-2} (*Ima*2) to -0.090×10^{-10} F m V^{-2} (*Pnma*) starts also to be visible for the highest values of electric field, that is above

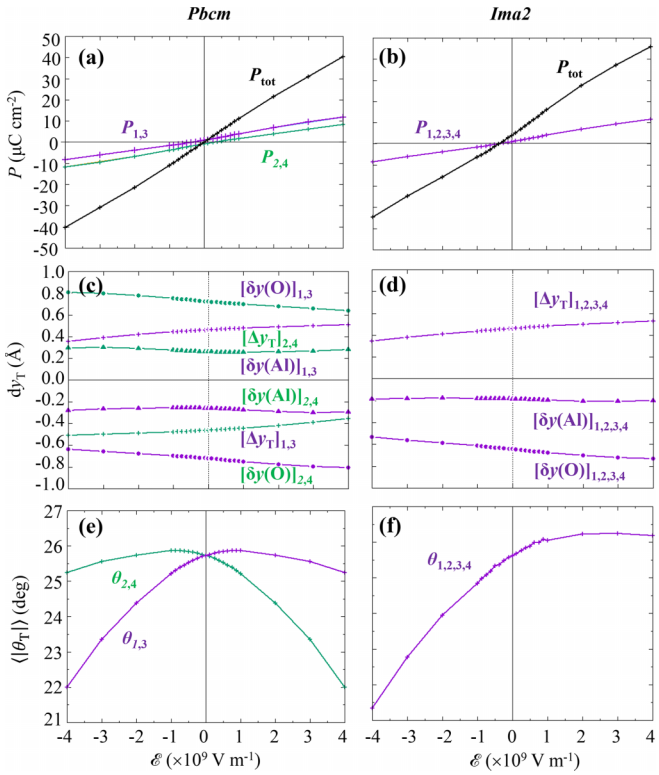

FIG. 6. Total and local electric polarization P_{tot} and P_α, respectively, as a function of the applied electric field $\mathcal{E}$ and calculated for the (a) *Pbcm* and (b) *Ima*2 phases. (c), (d) Atomic displacements and (e), (f) tetrahedra tilt angles $|\theta_T|$ also calculated as a function of $\mathcal{E}$.

10^9 V m^{-1}. The dielectric response is thus not expected to vary significantly depending on the stabilized crystallographic phase, even if we calculated slightly larger coefficients for the polar phases. On the contrary to the polar phases, such as the *Pbcm* structure, for polar phases like *Ima*2, we can note a small asymmetry of the curve, which is due to the non-null initial polarization P^0_{tot}, which is never reversed (each T chain preserves its initial handedness) due to the large energy barriers, as explained in the previous sections. The total electric polarization under the application of an electric field could indeed be expressed as a sum of the initial polarization P^0_{tot} and an induced polarization $P^{\text{ind}}_{\text{tot}}$: $P_{\text{tot}}(\mathcal{E}) = P^0_{\text{tot}} + P^{\text{ind}}_{\text{tot}}(\mathcal{E})$. The initial and spontaneous polarization P^0_{tot}, which is associated to the tetrahedra tilts, should stay quasiconstant. The induced polarization is associated to the linear ionic response to the electric field $P^{\text{ind}}_{\text{tot}}(\mathcal{E}) = \chi_i \varepsilon_0 \mathcal{E}$, with χ_i the ionic contribution to the electric susceptibility and ε_0 the vacuum permittivity. The free energy can then be rewritten as

$$F(\mathcal{E}) = F^0 - P^0_{\text{tot}}\mathcal{E} - \chi_i \varepsilon_0 \mathcal{E}^2. \quad (1)$$

For the *Ima*2 structure, we also performed a calculation using the density perturbation functional theory (DFPT) [47,48] to calculate the susceptibility and we found that $\chi\varepsilon_0 = 12.8 \times 10^{-11}$ F m^{-1} (χ being the total susceptibility), which is in good agreement with our previous estimation.

While P^0_{tot} can be parallel or antiparallel to the applied electric field, $P^{\text{ind}}_{\text{tot}}(\mathcal{E})$ will always be parallel to it. In consequence, if P^0_{tot} is parallel to the electric field, we expect that F will decrease as $\mathcal{E}$ increases, and the free energy of the polar phases will always be lower than the free energy of the nonpolar phases, the energy difference between the different phases being equal to the difference between their spontaneous polarization, multiplied by the magnitude of the electric field. If the spontaneous polarization is antiparallel to the electric field, the free energy will first increase until it reaches a maximum at $\mathcal{E} = -\frac{P^0_{\text{tot}}}{\chi_i \varepsilon_0}$, as shown in the inset of Fig. 4(a); at high electric-field values, the nonpolar phases will be the most stable.

According to the discussion above, we succeeded to understand why the polar or nonpolar phases could be more stable according to the direction of the applied electric field. From Eq. (1), if we consider that χ_i does not strongly vary for the different crystallographic phases, we should conclude that the difference of free energy between the different phases should vary linearly or remain constant if the two phases have initially the same electric polarization, which is not the case according to Fig. 4. Of course, we already saw that, at high electric field, the variation of the total electric polarization is not fully linear anymore. In order to have a better insight in the mechanisms that govern the change of electric polarization, we can decompose the total electric polarization in chain contributions P_α, as already done in Fig. 3(b). It is then possible to see in Figs. 6(a) and 6(b) that each P_α follows the same trend than P_{tot}. To improve the analysis, we also chose to show in Figs. 6(c) and 6(d) the atomic displacements and the corresponding cation-anion bucklings Δy_T, and in Figs. 6(e) and 6(f) the variation of the tetrahedra-tilt angles $|\theta_T|$ as a function of $\mathcal{E}$.

Let us first consider the *Ima*2 structure for simplicity. We can see that the cation-anion buckling along the [001] direction, $\langle \Delta y_T \rangle$, decreases by approximately 12 pm for each chain, when the electric field is antiparallel to the initial electric polarization and decreases from 0 to -4×10^9 V m^{-1}. We observe on the contrary a smaller increase by 7 pm, when the electric field is increased to $+4 \times 10^9$ V m^{-1}. This variation of buckling is mostly governed by the displacement of oxygen atoms. Concerning the tetrahedra-tilt angles, again we can observe a stronger variation when the electric field is applied antiparallel to the initial electric polarization than when it is parallel, with a maximum decrease (increase) of 5° (0.6°) in the considered electric-field range. The quasilinear variation of the local and total polarizations P_α and P_{tot} as a function of the electric field can thus be mostly ascribed to the linear response to the electric field, which results in a translation of cations and anions. The nonlinear component can partly be attributed to the small variations of tilt angles θ_T, which appear to be mostly quadratic. These variations of tilt angles as a function of $\mathcal{E}$ show that the spontaneous polarization arising from the tetrahedra tilts and that we first considered as constant, will display short variations, which may partly explain the nonlinear variation of P_{tot} at high electric field and why the difference of free energy between the different phases is also not linear. It is also important to keep in mind that $\langle \Delta y_T \rangle$ and $\langle |\theta_T| \rangle$ are quantities which are calculated from the Al-O atoms present in the T layers only, while the local electric polarization P_α are calculated in a volume including

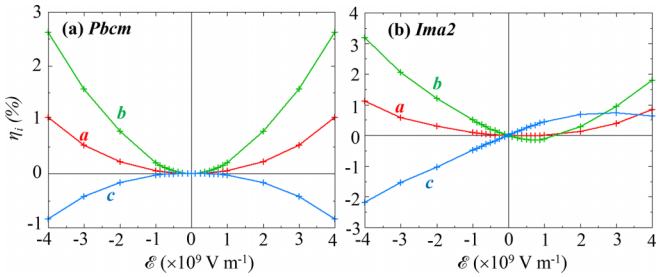

FIG. 7. Lattice strain η_i as a function of the applied electric field $\mathcal{E}$.

also surrounding atoms in consideration. These other sublattices will also undergo some distortions as it is already known to happen in perovskites.

Contrary to the *Ima*2 phase, for which all the T chains are equivalent, the *Pbcm* phase displays two sets of chains [Fig. 6(a)], one with the local spontaneous polarization P^0_α parallel and the other one antiparallel to the electric field, whatever its direction is. As it was noticed before, the behavior of each chain can be considered, at first, as independent. Their local polarizations present similar slopes than the chains in the *Ima*2 phase. We also observe the same trends for cation-anion bucklings and tetrahedra tilts, with mirror variations for the two sets of chains, due to the direction of their chain spontaneous polarization with respect to the electric field. If we analyze in more details the variations of P_α in the *Pbcm* phase, we can see that the slopes displayed by the two sets of chain is not exactly equal. We calculated that the polarization difference between two chains with opposite handedness, $P_1 - P_2$ for example, increases from 1.7 μC cm^{-2} to 3.4 μC cm^{-2}, when the electric field is increased between 0 and 4×10^9 V m^{-1}. It is certainly partly due to the asymmetric variation of the tilt angles $\langle|\theta_T|\rangle$.

3. Lattice strain

Let us finally investigate the effect of applying an electric field on the lattice parameters, as shown in Fig. 7. We will characterize the variations of lattice parameters thanks to first- and second-order coefficients d_i and M_i, respectively, obtained by fitting the lattice strain η as a function of $\mathcal{E}$ in a range between -10^9 and $+10^9$ V m^{-1}. These coefficients are reported in Table II. They may roughly correspond to converse piezoelectric and electrostrictive coefficients, but are mostly indicative as a precise calculation would require to use more accurate methods [49], which is beyond the scope of this paper. We define the lattice strain coefficients $\eta_i = (j - j_0)/j_0$, with $i = x, y, z$, $j = a, b, c$, and j_0 being the lattice parameter at zero electric field.

TABLE II. Piezoelectric and electrostrictive coefficients d_i and M_i calculated by fitting the variation of strain η_i as a function of an electric field $\mathcal{E}$ applied along the [010] direction and with a magnitude varying between -10^9 and $+10^9$ V m^{-1}. Because the electric polarization and applied electric fields are along y, $d_x = d_{21}$, $d_y = d_{22}$, and $d_z = d_{23}$, in Voigt notations [50].

Space group	M_x	M_y	M_z	d_x	d_y	d_z
	($\times 10^{-2}$ Å^2 V^{-2})			(pm V^{-1})		
Pbcm	5.00	20.28	−2.17			
Pnma	5.84	22.72	−4.82			
*Pmc*2$_1$	4.45	20.76	−3.10	−0.29	−1.68	2.41
*Ima*2	4.04	18.26	−1.47	−0.43	−3.30	4.71

For the nonpolar phases, such as the *Pbcm* structure [Fig. 7(a)], we fitted $\eta_i(\mathcal{E}) = M_i\mathcal{E}^2$ and we calculated a quasi-quadratic elongation of the in-plane lattice parameters, which is approximately four times bigger for the b lattice parameter than for a, recalling that the y axis is the direction of the electric field. The calculated large increase of the b lattice parameter is consistent with the increase of the electric polarization P_{tot} induced by the applied electric field. The elongation of in-plane lattice parameters is accompanied by a contraction of the out-of-plane lattice parameter c. The calculated coefficients thus reflect the anisotropic electrostrictive behavior (see Table II). In the previous subsection, we saw that the induced change of electric polarization could help to understand the (de)stabilization of polar phases over nonpolar phases. Concerning the relative stability of the two nonpolar phases *Pbcm* and *Pnma*, we also saw that their free energies remain very close, but that, from an electric field value of $\mathcal{E} = \pm 1.9 \times 10^9$ V m^{-1}, the *Pnma* phase becomes more stable than the *Pbcm* one. The calculated changes of lattice parameters could also explain this change of relative stability. Indeed, the *Pnma* phase could become more stable than the *Pbcm* structure because, when $|\mathcal{E}|$ increases, the decrease of c induces a consecutive increase of the interlayer chain interaction (which imposes an antiferroelectric ordering [16,25,26]), while the increase of the in-plane lattice parameter a, on the contrary, decreases the intralayer chain interaction.

When polar phases are stabilized [see Fig. 7(b) for the *Ima*2 structure], on the contrary to the *Pbcm* structure, the electric field will have a different effect depending if it is applied parallel (positive values) or antiparallel (negative) to the electric polarization at zero field P^0_{tot}. When the direction is antiparallel, the variation of lattice parameters follows the same trend than for the *Pbcm* phase, while, when it is parallel, we observe an increase of the out-of-plane lattice parameter c and a decrease of b, as the magnitude of $\mathcal{E}$ increases up to 1–2 $\times 10^9$ V m^{-1}. From Fig. 7(b), it is also possible to see that the variation of the c parameter as a function of $\mathcal{E}$, when $\mathcal{E}$ is low, is more linear than for the *Pbcm* phase. Because *Ima*2 is noncentrosymmetric, the piezoelectric coefficients are expected to be nonzero. For this phase, we thus fitted the lattice-parameter curves by $\eta_i(\mathcal{E}) = d_i\mathcal{E} + M_i\mathcal{E}^2$. We found that along y and z, the piezoelectric and electrostrictive coefficients display opposite signs and relatively large values, which suggests that they govern the strain variation at low electric fields.

Piezoelectric materials with negative longitudinal coefficients are relatively rare but have been reported in wurtzite BN [51], orthorhombic hafnia HfO_2 [52], *ABC* hexagonal ferroelectrics [53], or also in layered ferroelectrics like $CuInP_2S_6$ [54]. The piezoelectric coefficient can be decomposed into the sum of two terms, the clamped-ion term, which is the component calculated for the equilibrium structure, i.e., at zero strain, and the internal-strain term [53,55]. Negative

piezoelectric coefficients have been found when the clamped-ion term is negative and dominates over the second term [53,54], generally because this last one is small due to low Born effective charges or to small responses associated to the atomic positions, which can be the case in low-dimensional crystals [54]. On the contrary, in HfO_2, the lattice-mediated response has been found to dominate and to be at the origin of the negative coefficient. For $Ca_2Al_2O_5$, we calculated that the longitudinal coefficient coming from the ionic response d_y is negative. This ionic term depends on the calculated Born effective charges, given in Appendix A, which are not particularly small, with diagonal terms close to $\sim \pm 2e$, and on the variation of structural distortions, which on the contrary, can be small if the electric field is parallel to the spontaneous polarization [Figs. 6(d) and 6(f)]. We then decided to perform a direct calculation of the piezoelectric stress coefficient, first in order to confirm this coefficient, which has been calculated by fitting the variation of strain over a wide range of electric field $\mathcal{E}$, and second to verify if the total piezoelectric coefficient, including the purely electronic contribution, is also negative or not. To do so, we applied the DFPT to the *Ima*2 structure calculated at $\mathcal{E} = 0$ V m^{-1} and we calculated the piezoelectric stress coefficients $e_{ij} = \frac{\delta P_i}{\delta \eta_i}$. We found ion-clamped terms equal to $\bar{e}_{22} = +15.3$ μC cm^{-2} (in Voigt notations) and $\bar{e}_{23} = -8.7$ μC cm^{-2}, which are much smaller than the ionic terms, calculated using finite-difference approach $e'_{22} = -53.3$ μC m^{-2} and $e'_{23} = 73.2$ μC cm^{-2}. This calculation thus confirms that the lattice-mediated contribution to the piezoelectric coefficients dominates and is responsible for a negative total piezoelectric coefficient. From the full set of coefficients e_{ij}, it is possible to calculate the total converse piezoelectric charge coefficients (see Table III in Appendix C) $d_{22} = -2.88$ pm V^{-1} and $d_{23} = 4.58$ pm V^{-1}, which are close from the ionic terms d_y and d_z reported in Table II.

IV. CONCLUSION

With our first-principles calculations, we found that the ground state of the brownmillerite oxide $Ca_2Al_2O_5$ corresponds to the nonpolar phase of space group *Pbcm*, associated with an antiferroelectric ordering and chains of oxygen tetrahedra having alternatively opposite handednesses along the [100] direction. In addition to this ground state, several other phases with close internal energies can be formed by changing the distribution of chain handednesses. This richness of phase diagrams mostly comes from the relatively low structural coupling between the different chains. The second most stable phase is calculated to be the ferroelectric *Ima*2 phase; this phase was experimentally observed at room temperature, which might be a consequence of the needed high temperature and pressures to grow $Ca_2Al_2O_5$. The calculated low electric polarization in $Ca_2Al_2O_5$ is close from the one measured in $Sr_2Fe_2O_5$ [3] and strategies would thus have to be developed in order to make such ferroelectric materials interesting for potential applications. Applying a strain is, for example, often envisioned to increase the electric polarization, but, as already shown by Young and Rondinelli [5] and by our calculations, the strain response in brownmillerite may be difficult to predict without a thorough study because of the strong coupling with the tetrahedra tilts.

At low temperature and without any external electric field, it appears that once one of the four considered phases is stabilized, it should remain robust owing to the high-energy barrier (in the order of $\sim$1 eV per chain of two tetrahedra), which have to be overpassed in order to switch between different phases, by changing one chain handedness. From the calculated barriers, we can conclude that the switching between different phases will generally require to go through intermediate states and to reverse the chain polarization one by one. At this stage, it is not possible to know if these reversals will be random or associated to the displacements of domain boundaries. We, however, found that the reversal of consecutive chains is slightly easier when the chains are lying in the same (001) atomic layer. In any case, because of the calculated high-energy barrier to overpass, we proposed that *Ima*2 polar phases could be more easily stabilized by applying an electric field at high temperature and then slowly cooling down the crystal to preserve the phase at room temperature. Such method could provide an additional way to ensure the stabilization of polar phases in brownmillerite structures, in addition to the control of other parameters such as epitaxial strain.

We finally discussed the variation of strain as a function of the external electric field applied along the T-chain directions. We found that, due to the electrostrictive behavior, which will change the interlayer distances, or in other words the lattice coupling between the different chains, the electric field could help to stabilize different nonpolar phases. When a polar phase is stabilized, we predict that, because of its low lattice response, $Ca_2Al_2O_5$ possesses a negative longitudinal piezoelectric coefficient in the direction parallel to the field.

We chose to focus our study on the nonmagnetic $Ca_2Al_2O_5$ brownmillerite. We can expect that the results and mechanisms described in this paper would remain qualitatively valid for other compounds, more suitable for applicative purposes, such as $Sr_2Fe_2O_5$ or $Sr_2Co_2O_5$. Because we found that the energy barrier to transit between different crystallographic phases is of the same order of magnitude than the energy barrier for one oxygen atom to move between two atomic sites [15,45], it would be interesting to extend this study in order to try to understand if a coupling can exist between these two processes, to verify if the oxygen conductivity can be facilitated by the stabilization of a particular crystallographic phase or if the mobility of atoms can be concomitant with the switching between different phases. Finally, another continuation to this work would be to investigate the effect of an electric field applied in directions perpendicular to the chains of oxygen tetrahedra, in order to see if it can allow to stabilize new phases or to understand how it could help to rotate the chains' direction [7].

ACKNOWLEDGMENTS

This work was granted access to the HPC resources of CALMIP (Allocation No. 2021-2023/P19004). L.B. thanks the support from Vannevar Bush Faculty Fellowship (VBFF) Grant No. N00014-20-1-2834 from the Department

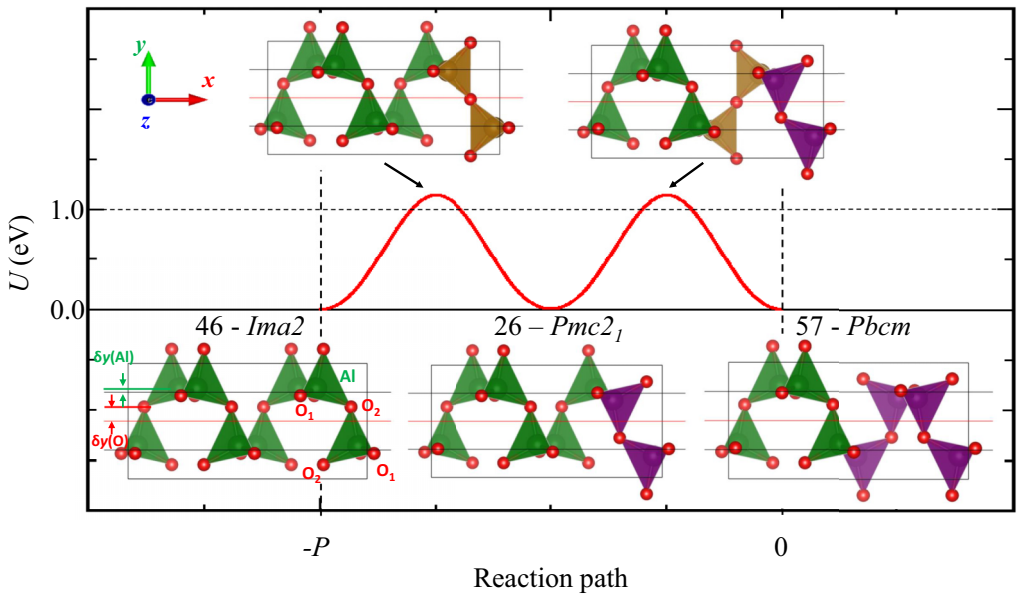

FIG. 8. Atomic structures [projected on a (001) plane] calculated with the NEB method for the $46(-P) \rightarrow 26 \rightarrow 57 \rightarrow 26 \rightarrow 46(+P)$ reaction path given in Fig. 2. Only half of the reaction path is shown as it is symmetrical when no electric field is applied.

of Defense and ONR Grant No. N00014-21-1-2086. The authors would like to thank G. Dezanneau for useful discussions.

APPENDIX A: BORN EFFECTIVE CHARGES

The Born effective charges Z^* (in e) calculated for every atom using the centrosymmetric structure *Imma* are

$$Z^*(\mathrm{Ca}) = \begin{pmatrix} 2.65495 & 0 & 0.01310 \\ 0 & 2.50003 & 0 \\ -0.00592 & 0 & 2.18606 \end{pmatrix},$$

$$Z^*(\mathrm{Al_T}) = \begin{pmatrix} 2.24139 & 0 & 0 \\ 0 & 2.33007 & 0 \\ 0 & 0 & 2.76508 \end{pmatrix},$$

$$Z^*(\mathrm{Al_O}) = \begin{pmatrix} 3.04751 & 0 & 0.07125 \\ 0 & 2.92637 & 0 \\ 0.06968 & 0 & 2.97150 \end{pmatrix},$$

$$Z^*(\mathrm{O_{Ca}}) = \begin{pmatrix} -1.97569 & 0 & \pm 0.19361 \\ 0 & -1.70541 & 0 \\ \pm 0.17645 & 0 & -2.38144 \end{pmatrix},$$

$$Z^*(\mathrm{O_{Al_T}}) = \begin{pmatrix} -1.88292 & \pm 0.42739 & 0 \\ \pm 0.48843 & -2.19961 & 0 \\ 0 & 0 & -1.82320 \end{pmatrix},$$

$$Z^*(\mathrm{O_{Al_O}}) = \begin{pmatrix} -2.37623 & \pm 0.10791 & \pm 0 \\ \pm 0.14031 & -2.31655 & 0 \\ \pm 0 & 0 & -1.75623 \end{pmatrix}.$$

APPENDIX B: BORN EFFECTIVE CHARGES

In Fig. 8, we displayed the atomic structures corresponding to the minima and maxima calculated along the $46(-P) \rightarrow 26 \rightarrow 57 \rightarrow 26 \rightarrow 46(+P)$ reaction path. As it can be seen in this figure, the T chains are rotated one by one and the barrier energy maxima correspond to tetrahedra tilts angles $\theta_T = 0°$. Looking more closely at the atomic structure, we can see that the rotation of the tetrahedra induces a small variation of the Al position along the [010] δy(Al), while the stronger variation of δy(O) is mostly governed by the displacement of the O_2 atoms, which are linking the different tetrahedra of a given chain (see Fig. 8). When $\theta_T = 0°$, the oxygen atoms O_2 are located in-between the two Al atoms, i.e. where the space which separates them is minimum, thus resulting in an increase of the b lattice parameter by 0.04 Å and a local maximum of the energy U along the NEB reaction path.

TABLE III. Stress piezoelectric coefficients e_{ij} and converse piezoelectric coefficients d_{ij} calculated directly from DFT, for the ferroelectric phase *Ima*2. The coefficients are given in Voigt notations [50].

ij	$\bar{e}_{ij}$ μC cm^{-2}	e'_{ij} μC cm^{-2}	d_{ij} pm V^{-1}
21	−7.8	27.4	−0.899
22	15.3	−53.3	−2.883
23	−8.7	73.2	4.577
35	−7.5	48.2	4.504
16	−7.0	13.9	0.987

APPENDIX C: PIEZOELECTRIC COEFFICIENTS AND ELASTIC CONSTANTS

We performed calculations of the converse piezoelectric coefficients $d_{ij} = \frac{\delta \eta_i}{\delta \mathcal{E}_j}$ and the stress piezoelectric coefficients $e_{ij} = \frac{\delta P_i}{\delta \eta_j}$, which are labeled following Voigt notations [50]. The ion-clamped $\bar{e}_{ij}$ and internal-strain terms e'_{ij} are calculated from the DFPT [47,48] and finite differences. The d_{ij} coefficients are related to e_{ik} through the elastic compliances S_{kj} [47,52]:

$$d_{ij} = \frac{\delta P_i}{\delta \eta_j} = e_{ik}(C^{-1})_{kj} = e_{ik}S_{kj} \tag{C1}$$

with C_{kj} being the elastic constants.

The coefficients calculated for the *Ima*2 structure are summarized in Table III.

[1] M. T. Anderson, J. T. Vaughey, and K. R. Poeppelmeier, Structural similarities among oxygen-deficient perovskites, Chem. Mater. **5**, 151 (1993).

[2] J. Young, E. J. Moon, D. Mukherjee, G. Stone, V. Gopalan, N. Alem, S. J. May, and J. M. Rondinelli, Polar oxides without inversion symmetry through vacancy and chemical order, J. Am. Chem. Soc. **139**, 2833 (2017).

[3] K. T. Kang, C. J. Roh, J. Lim, T. Min, J. H. Lee, K. Lee, T. Y. Lee, S. Kang, D. Seol, J. Kim, H. Ohta, A. Khare, S. Park, Y. Kim, S. C. Chae, Y. S. Oh, J. Lee, J. Yu, J. S. Lee, and W. S. Choi, A room-temperature ferroelectric ferromagnet in a 1D tetrahedral chain network, Adv. Mater. **31**, 1808104 (2019).

[4] H. Tian, L. Bellaiche, and Y. Yang, Diversity of structural phases and resulting control of properties in brownmillerite oxides: A first-principles study, Phys. Rev. B **100**, 220103(R) (2019).

[5] J. Young and J. M. Rondinelli, Crystal structure and electronic properties of bulk and thin film brownmillerite oxides, Phys. Rev. B **92**, 174111 (2015).

[6] A. Khare, J. Lee, J. Park, G.-Y. Kim, S.-Y. Choi, T. Katase, S. Roh, T. S. Yoo, J. Hwang, H. Ohta, J. Son, and W. S. Choi, Directing oxygen vacancy channels in $SrFeO_{2.5}$ epitaxial thin films, ACS Appl. Mater. Interfaces **10**, 4831 (2018).

[7] L. Zhu, L. Gao, L. Wang, Z. Xu, J. Wang, X. Li, L. Liao, T. Huang, H. Huang, A. Ji, N. Lu, Z. Cao, Q. Li, J.-R. Sun, P. Yu, and X. Bai, Atomic-scale observation of structure transition from brownmillerite to infinite layer in $SrFeO_{2.5}$ thin films, Chem. Mater. **33**, 3113 (2021).

[8] H. Han, A. Sharma, H. L. Meyerheim, J. Yoon, H. Deniz, K.-R. Jeon, A. K. Sharma, K. Mohseni, C. Guillemard, M. Valvidares, P. Gargiani, and S. S. P. Parkin, Control of oxygen vacancy ordering in brownmillerite thin films via ionic liquid gating, ACS Nano **16**, 6206 (2022).

[9] M. A. Hayward and M. J. Rosseinsky, Cool conditions for mobile ions, Nature (London) **450**, 960 (2007).

[10] W. Paulus, H. Schober, S. Eibl, M. Johnson, T. Berthier, O. Hernandez, M. Ceretti, M. Plazanet, K. Conder, and C. Lamberti, Lattice dynamics to trigger low temperature oxygen mobility in solid oxide ion conductors, J. Am. Chem. Soc. **130**, 16080 (2008).

[11] H. Jeen, W. S. Choi, J. W. Freeland, H. Ohta, C. U. Jung, and H. N. Lee, Topotactic phase transformation of the brownmillerite $SrCoO_{2.5}$ to the perovskite $SrCoO_{3-\delta}$, Adv. Mater. **25**, 3651 (2013).

[12] V. R. Nallagatla, T. Heisig, C. Baeumer, V. Feyer, M. Jugovac, G. Zamborlini, C. M. Schneider, R. Waser, M. Kim, C. U. Jung, and R. Dittmann, Topotactic phase transition driving memristive behavior, Adv. Mater. **31**, 1903391 (2019).

[13] J. Tian, H. Wu, Z. Fan, Y. Zhang, S. J. Pennycook, D. Zheng, Z. Tan, H. Guo, P. Yu, X. Lu, G. Zhou, X. Gao, and J.-M. Liu, Nanoscale topotactic phase transformation in $SrFeO_x$ epitaxial thin films for high-density resistive switching memory, Adv. Mater. **31**, 1903679 (2019).

[14] M. S. Saleem, B. Cui, C. Song, Y. Sun, Y. Gu, R. Zhang, M. U. Fayaz, X. Zhou, P. Werner, S. S. P. Parkin, and F. Pan, Electric field control of phase transition and tunable resistive switching in $SrFeO_{2.5}$, ACS Appl. Mater. Interfaces **11**, 6581 (2019).

[15] X. Mou, J. Tang, Y. Lyu, Q. Zhang, S. Yang, F. Xu, W. Liu, M. Xu, Y. Zhou, W. Sun, Y. Zhong, B. Gao, P. Yu, H. Qian, and H. Wu, Analog memristive synapse based on topotactic phase transition for high-performance neuromorphic computing and neural network pruning, Sci. Adv. **7**, eabh0648 (2021).

[16] T. G. Parsons, H. D'Hondt, J. Hadermann, and M. A. Hayward, Synthesis and structural characterization of $La_{1-x}A_xMnO_{2.5}$ (A = Ba, Sr, Ca) phases: Mapping the variants of the Brownmillerite structure, Chem. Mater. **21**, 5527 (2009).

[17] H. Tian, X.-Y. Kuang, A.-J. Mao, Y. Yang, H. Xiang, C. Xu, S. O. Sayedaghaee, J. Íñiguez, and L. Bellaiche, Novel type of ferroelectricity in brownmillerite structures: A first-principles study, Phys. Rev. Mater. **2**, 084402 (2018).

[18] A. P. Levanyuk and D. G. Sannikov, Improper ferroelectrics, UFN **112**, 561 (1974) [Sov. Phys. Usp. **17**, 199 (1974)].

[19] E. Bousquet, M. Dawber, N. Stucki, C. Lichtensteiger, P. Hermet, S. Gariglio, J.-M. Triscone, and P. Ghosez, Improper ferroelectricity in perovskite oxide artificial superlattices, Nature (London) **452**, 732 (2008).

[20] N. A. Benedek and C. J. Fennie, Hybrid Improper Ferroelectricity: A Mechanism for Controllable Polarization-Magnetization Coupling, Phys. Rev. Lett. **106**, 107204 (2011).

[21] A. T. Mulder, N. A. Benedek, J. M. Rondinelli, and C. J. Fennie, Turning ABO_3 antiferroelectrics into ferroelectrics: Design rules for practical rotation-driven ferroelectricity in double perovskites and $A_3B_2O_7$ Ruddlesden-Popper compounds, Adv. Funct. Mater. **23**, 4810 (2013).

[22] H. J. Zhao, J. Íñiguez, W. Ren, X. M. Chen, and L. Bellaiche, Atomistic theory of hybrid improper ferroelectricity in perovskites, Phys. Rev. B **89**, 174101 (2014).

[23] J. Holakovský, A new type of the ferroelectric phase transition, Phys. Status Solidi B **56**, 615 (1973).

[24] I. A. Kornev and L. Bellaiche, Nature of the ferroelectric phase transition in multiferroic $BiFeO_3$ from first principles, Phys. Rev. B **79**, 100105(R) (2009).

[25] A. M. Abakumov, A. S. Kalyuzhnaya, M. G. Rozova, E. V. Antipov, J. Hadermann, and G. Van Tendeloo, Compositionally induced phase transition in the $Ca_2MnGa_{1-x}Al_xO_5$ solid solu-

tions: Ordering of tetrahedral chains in brownmillerite structure, Solid State Sci. **7**, 801 (2005).

[26] J. Hadermann, A. M. Abakumov, H. D'Hondt, A. S. Kalyuzhnaya, M. G. Rozova, M. M. Markina, M. G. Mikheev, N. Tristan, R. Klingeler, B. Büchner, and E. V. Antipov, Synthesis and crystal structure of the $Sr_2Al_{1.07}Mn_{0.93}O_5$ brownmillerite, J. Mater. Chem. **17**, 692 (2007).

[27] S. Lambert, H. Leligny, D. Grebille, D. Pelloquin, and B. Raveau, Modulated distribution of differently ordered tetrahedral chains in the brownmillerite structure, Chem. Mater. **14**, 1818 (2002).

[28] H. Krüger and V. Kahlenberg, Incommensurately modulated ordering of tetrahedral chains in $Ca_2Fe_2O_5$ at elevated temperatures, Acta Crystallogr. Sect. B **61**, 656 (2005).

[29] B. Lazic, H. Krüger, V. Kahlenberg, J. Konzett, and R. Kaindl, Incommensurate structure of $Ca_2Al_2O_5$ at high temperatures – structure investigation and Raman spectroscopy, Acta Crystallogr. Sect. B **64**, 417 (2008).

[30] H. Fu and L. Bellaiche, First-Principles Determination of Electromechanical Responses of Solids under Finite Electric Fields, Phys. Rev. Lett. **91**, 057601 (2003).

[31] P. Hohenberg and W. Kohn, Inhomogeneous electron gas, Phys. Rev. **136**, B864 (1964).

[32] W. Kohn and L. J. Sham, Self-consistent equations including exchange and correlation effects, Phys. Rev. **140**, A1133 (1965).

[33] G. Kresse and J. Hafner, Ab initio molecular-dynamics simulation of the liquid-metalamorphous-semiconductor transition in germanium, Phys. Rev. B **49**, 14251 (1994).

[34] G. Kresse and J. Furthmüller, Efficient iterative schemes for ab initio total-energy calculations using a plane-wave basis set, Phys. Rev. B **54**, 11169 (1996).

[35] P. E. Blöchl, Projector augmented-wave method, Phys. Rev. B **50**, 17953 (1994).

[36] J. P. Perdew, A. Ruzsinszky, G. I. Csonka, O. A. Vydrov, G. E. Scuseria, L. A. Constantin, X. Zhou, and K. Burke, Restoring the Density-Gradient Expansion for Exchange in Solids and Surfaces, Phys. Rev. Lett. **100**, 136406 (2008); **102**, 039902(E) (2009).

[37] H. J. Monkhorst and J. D. Pack, Special points for Brillouin-zone integrations, Phys. Rev. B **13**, 5188 (1976).

[38] G. Henkelman, B. P. Uberuaga, and H. Jónsson, A climbing image nudged elastic band method for finding saddle points and minimum energy paths, J. Chem. Phys. **113**, 9901 (2000).

[39] P. Aggarwal, J. Gard, F. Glasser, and G. Biggar, Synthesis and properties of dicalcium aluminate, $2CaO.Al_2O_3$, Cement Concrete Res. **2**, 291 (1972).

[40] V. Kahlenberg, R. X. Fischer, and C. S. J. Shaw, Rietveld analysis of dicalcium aluminate ($Ca_2Al_2O_5$) – A new high pressure phase with the Brownmillerite-type structure, Am. Mineral. **85**, 1061 (2000).

[41] G. Hentschel, Mayenit, $12CaO{\cdot}7Al_2O_3$, und brownmillerit, $2CaO{\cdot}(Al,Fe)_2O_3$, zwei neue Minerale in den Kalksteinschlüssen der Lava des Ettringer Bellerberges, Neues Jahrb. für Mineral. Monatshefte **1964**, 22 (1964).

[42] H. Taylor, *Cement Chemistry,* 2nd ed. (Thomas Telford, London, 1997).

[43] G. J. Redhammer, G. Tippelt, G. Roth, and G. Amthauer, Structural variations in the brownmillerite series $Ca_2(Fe_{2-x}Al_x)O_5$: Single-crystal x-ray diffraction at 25 °C and high-temperature x-ray powder diffraction (25 °C $\leqslant T \leqslant$ 1000 °C), Am. Mineral. **89**, 405 (2004).

[44] X. Y. Li, Q. Yang, J. X. Cao, L. Z. Sun, Q. X. Peng, Y. C. Zhou, and R. X. Zhang, Domain wall motion in perovskite ferroelectrics studied by the nudged elastic band method, J. Phys. Chem. C **122**, 3091 (2018).

[45] U. Matsumoto, A. Kuwabara, C. A. J. Fisher, H. Moriwake, and I. Tanaka, Oxide-ion diffusion in brownmillerite-type $Ca_2AlMnO_{5+\delta}$ from first-principles calculations, Phys. Chem. Chem. Phys. **24**, 1503 (2022).

[46] D.-H. Choe, S. Kim, T. Moon, S. Jo, H. Bae, S.-G. Nam, Y. S. Lee, and J. Heo, Unexpectedly low barrier of ferroelectric switching in HfO_2 via topological domain walls, Mater. Today **50**, 8 (2021).

[47] X. Wu, D. Vanderbilt, and D. R. Hamann, Systematic treatment of displacements, strains, and electric fields in density-functional perturbation theory, Phys. Rev. B **72**, 035105 (2005).

[48] M. Gajdoš, K. Hummer, G. Kresse, J. Furthmüller, and F. Bechstedt, Linear optical properties in the projector-augmented wave methodology, Phys. Rev. B **73**, 045112 (2006).

[49] D. S. P. Tanner, E. Bousquet, and P.-E. Janolin, Optimized methodology for the calculation of electrostriction from first-principles, Small **17**, 2103419 (2021).

[50] J. F. Nye, *Physical Properties of Crystals: Their Representation by Tensors and Matrices*, Oxford Science Publications (Clarendon, Oxford, 1985).

[51] K. S. Suzuki and H. O. H. Okumura, First-principles study on piezoelectric constants in strained BN, AlN, and GaN, Jpn. J. Appl. Phys. **37**, L1421 (1998).

[52] S. Dutta, P. Buragohain, S. Glinsek, C. Richter, H. Aramberri, H. Lu, U. Schroeder, E. Defay, A. Gruverman, and J. Íñiguez, Piezoelectricity in hafnia, Nat. Commun. **12**, 7301 (2021).

[53] S. Liu and R. E. Cohen, Origin of Negative Longitudinal Piezoelectric Effect, Phys. Rev. Lett. **119**, 207601 (2017).

[54] Y. Qi and A. M. Rappe, Widespread Negative Longitudinal Piezoelectric Responses in Ferroelectric Crystals with Layered Structures, Phys. Rev. Lett. **126**, 217601 (2021).

[55] G. Sághi-Szabó, R. E. Cohen, and H. Krakauer, First-Principles Study of Piezoelectricity in $PbTiO_3$, Phys. Rev. Lett. **80**, 4321 (1998).